Original paper

Predicting TNFRSF4 expression and prognosis in head and neck squamous cell carcinoma tissue: a pathological image analysis approach

Weiming Chu[1], Chen Chu[1], Zongmei Ding[2], Wei Guan[1], Shiyuan Li[1], Jixin Jiang[2], Yu Xue[1], Jianping Qiu[1], Aijun Guo[1]

[1]Department of Stomatology, Northern Jiangsu People's Hospital, P.R. China
[2]CDepartment of Pathology, Northern Jiangsu People's Hospital, P.R. China

Head and neck squamous cell carcinoma (HNSCC) exhibits a poor 5-year survival rate. TNFRSF4 is gaining attention in tumor therapy. The objective of this study was to forecast the expression of TNFRSF4 in HNSCC tissue using analysis of pathological images and investigate its possible molecular mechanisms.

Transcriptome, clinical, and pathological data of HNSCC patients from the TCGA database were analyzed. Features were extracted with PyRadiomics for support vector machine model development. The evaluation of model performance was conducted using ROC curve, calibration curve, and decision curve analyses. The correlation between pathomics score (PS), patient prognosis, and immune-related genes was assessed.

TNFRSF4 expression was significantly higher in the tumor group and independently associated with HNSCC prognosis. Features were extracted to build a predictive model for TNFRSF4, which demonstrated strong performance. PS correlated positively with immune-related genes.

This research highlights the potential of TNFRSF4 as a prognostic factor and demonstrates the utility of PS in relation to immune-related genes.

Key words: machine learning models, pathomics, TNFRSF4, HNSCC, prognosis.

Introduction

Around 90% of head and neck tumors are made up of head and neck squamous cell carcinoma (HNSCC) [1]. The current treatment strategy for HNSCC involves a combination of surgery, radiotherapy, and chemotherapy. Nevertheless, the survival rate of patients over a period of 5 years remains alarmingly low, as around 50% of individuals do not survive this period [2, 3]. The traditional prognostic indicators for HNSCC, including clinical pathological features and presence of human papillomavirus (HPV), are proving inadequate for meeting the demands of precision medicine. Hence, it is imperative to discover novel predictive indicators that can categorize patient prognosis and offer crucial perspectives for tailored precision treatment [4, 5].

TNFRSF4, also called OX40 or CD134, is a member of the tumor necrosis factor receptor superfamily and is expressed on various immune cells including activated T cells, B cells, macrophages, and dendritic cells [6]. The activation of T cells and the promotion of their proliferation and differentiation into functional effector T cells (CD4+ and CD8+ T cells) are significantly influenced by TNFRSF4. This activation enhances the immune response against infection and tumor cells, while also reversing the tumor cell inhibition of T cell activation and function. When TNFRSF4 binds to antigens associated with tumors, it stimulates T cells to produce an immune response, resulting in a higher quantity of T cells specific to the tumor and improving their ability to destroy tumor cells. Studies have examined the presence of TNFRSF4 expression in breast cancer, melanoma, and lymphoma. A significant correlation has been observed between elevated TNFRSF4 levels and extended survival in individuals diagnosed with colorectal cancer [7]. Additionally, TNFRSF4 inhibition has demonstrated noteworthy anti-cancer properties in breast cancer, melanoma, and various other malignancies [8]. Numerous clinical trials are currently being conducted to investigate the efficacy of combining TNFRSF4-targeted immunotherapy in various cancer types. For instance, one trial (NCT02221960) is exploring the potential synergistic anti-tumor immune responses in recurrent or metastatic solid tumors by combining the PD-L1 inhibitor durvalumab and the OX40 agonist. This indicates the considerable potential of TNFRSF4 for treating tumor cells and their microenvironment in the context of HNSCC, and the morphological features of HNSCC tissue can provide essential information for understanding HNSCC tumor cells and their microenvironment.

Currently, the detection of TNFRSF4 expression levels relies on peripheral blood cytokine detection, or protein levels testing using fresh or paraffin-embedded tissue samples. Nevertheless, hematoxylin and eosin (H&E) staining is crucial for clinical diagnosis and offers easily accessible image data. The field of pathology is gradually adopting artificial intelligence technology, which has a significant impact. Pathomics utilizes artificial intelligence to convert pathology images into extensive, high-quality data, enabling the examination of quantitative attributes such as texture, shape, edge gradient, and biological properties. This technique is utilized for the quantitative diagnosis of diseases, analysis of molecular expression, and prediction of disease outcomes [9–11].

Based on these factors, the study suggests a novel method to forecast TNFRSF4 expression in HNSCC tissues. This involves the utilization of histopathology techniques along with bioinformatics analysis to investigate the underlying molecular mechanisms.

Material and methods

Data resource and inclusion and exclusion criteria

Data from transcriptome sequencing and clinical follow-up of 528 patients diagnosed with HNSCC were collected retrospectively from the TCGA database (https://tcga-data.nci.nih.gov/tcga/). Patients eligible for the study had to fulfill the following requirements: (a) they were pathologically confirmed to have primary HNSCC and had undergone initial treatment; (b) they possessed adequate survival data and had survived for a minimum of 30 days; (c) they did not have any incomplete clinical variables; and (d) they had primary solid tumors with accessible sequencing data. Ultimately, data from 475 HNSCC cases were obtained. Furthermore, a total of 450 HNSCC pathology tissue samples accompanied by H&E images were obtained from the TCGA database at https://portal.gdc.cancer.gov/. The inclusion criteria for these images were: (a) excluding images of insufficient quality; and (b) selecting images that intersected with the aforementioned clinical data. In the end, a total of 271 pathological histology images from HNSCC patients were obtained. The Ethics Committee of Northern Jiangsu People's Hospital Affiliated to Yangzhou University (ethics, 2022ky036) has reviewed and granted approval for this study that includes human clinical specimens. The Institutional Review Board of our hospital approved and ensured compliance with the relevant guidelines and regulations for all methods and analysis.

Pathologic image acquisition, processing and segmentation

Histopathological tissue slides in the svs format, which had been formalin-fixed and paraffin-embedded, were downloaded from the TCGA database. The slides had a maximum magnification of 20× or 40×.

The tissue regions of the pathology slides were obtained using the OTSU algorithm, also known as the maximum interclass variance method, a thresholding algorithm employed for image binarization. The images were separated by the algorithm into undesired background areas and desired tissue regions. The images with a magnification of 40x were divided into several sub-images, each measuring 1024 × 1024 pixels. For the 20x magnification pictures, they were divided into numerous smaller images measuring 512 × 512 pixels, which were later enlarged to 1024 × 1024 pixels. Pathologists reviewed these sub-images to exclude poor quality ones, such as those with contamination, blurriness, or blank regions exceeding 50%. Ten random sub-images were chosen for subsequent analysis from every pathology image.

Feature extraction

PyRadiomics, an open-source Python package, was utilized to process the sub-images. This package standardized the images and extracted a grand total of 93 unique features, encompassing both first-order and second-order characteristics. Furthermore, advanced characteristics (Wavelet LL, LH, HL, HH) were obtained, leading to a grand total of 465 features. The histopathological features for subsequent data analysis were obtained by computing the average values of the features extracted from the ten sub-images of each patient's pathology image.

Feature selection

At first, the mRMR algorithm was used to select features with maximum relevance and minimum redundancy. This algorithm considers both the correlation between features and the variable to be predicted, as well as the correlation among different features. The measurement standard used is mutual information. The mRMR method calculates the correlation of the feature subset with the class by averaging the information gain of each feature with the class. To calculate redundancy among features, the mutual information between features is added together and then divided by the square of the number of features in the subset. Afterward, recursive feature elimination (RFE) was used for further feature selection. Predictive factors are ranked before modeling, and the less significant factors are progressively eliminated. The goal is to identify a subset of predictors that can generate a precise model. The model is trained continuously, removing n less important features after each training iteration and re-training with the remaining features to obtain new feature importance. This process is repeated until the optimal feature subset is obtained. The mRMR method selected the top 30 features, which were then further refined using RFE for feature selection. Figure 1 provides an overview of the entire architecture of the study.

Statistical analysis and machine learning

We obtained and processed the RNAseq data from the TCGA-HNSCC project using the STAR workflow from the TCGA database, and the data were extracted in FPKM format. For data visualization, the Mann-Whitney *U* test (Wilcoxon rank sum test) and the ggplot2 package were employed in the statistical analysis. The Kaplan-Meier survival plot was utilized to demonstrate variations in survival percentages across various cohorts, while the log-rank test was employed to evaluate the significance of these survival percentages. Furthermore, the Cox proportional hazards model was employed to investigate the correlation between study variables and

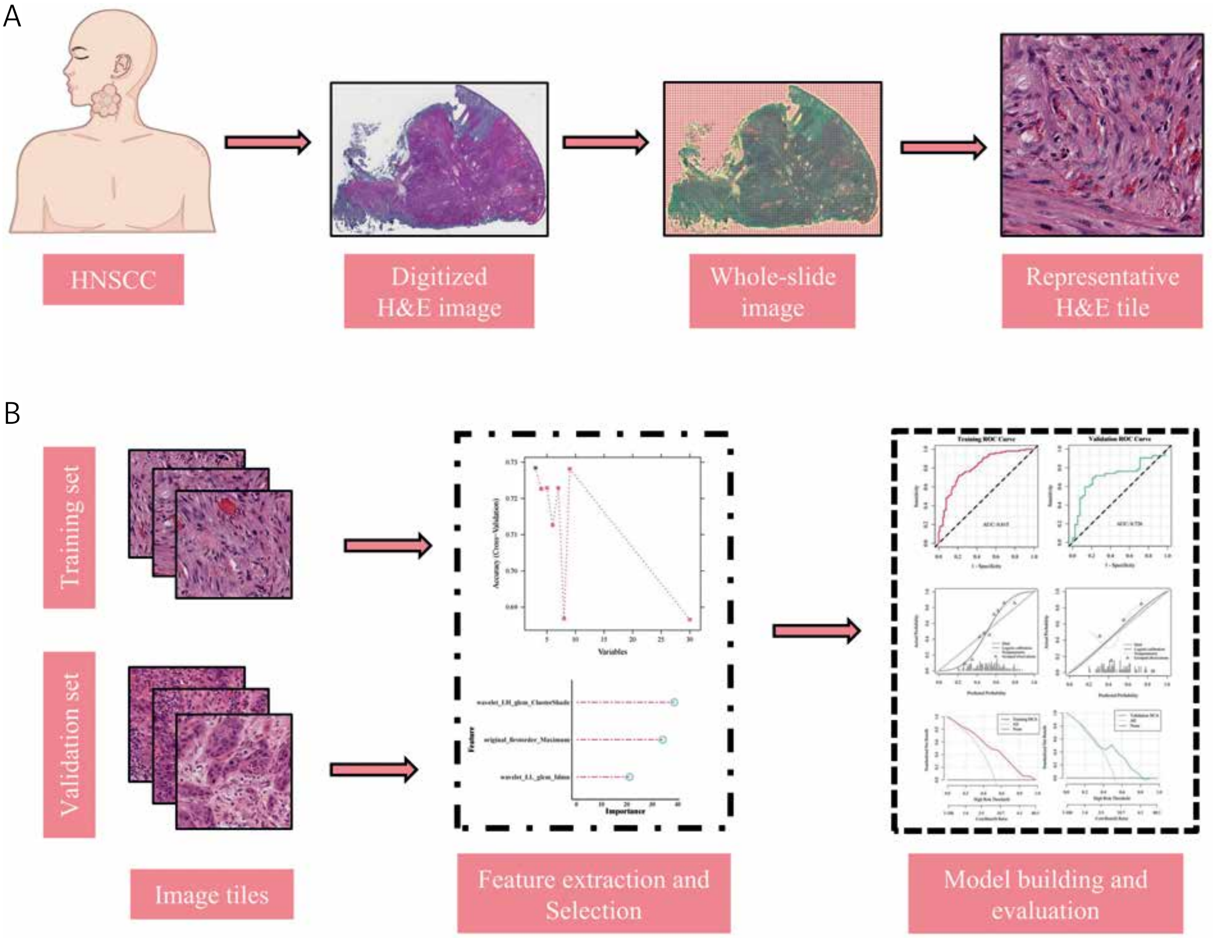

Fig. 1. Workflow of histopathological image analysis and modeling. **A**) A total of 271 H&E-stained images from patients were included in the study. From each image, 10 random regions were selected, each with a field of view measuring 1024 × 1024 pixels. **B**) The dataset was divided randomly into training and validation sets, with a ratio of 7 : 3. Pathomics features were extracted from histopathological image patches stained with H&E. The model was then trained using the training set and validated using the validation set

survival results, encompassing both single-factor and multiple-factor Cox regression analyses. In order to evaluate the effect of TNFRSF4 on patient prognosis, we performed single-factor Cox regression and likelihood ratio tests to examine the correlation between TNFRSF4 expression and other covariates. The GBM algorithm was employed to forecast gene expression using chosen pathological and histological characteristics, and the model's performance was assessed using different metrics such as precision, recall, specificity, and positive and negative predictive values. To assess the model's performance, the receiver operating characteristic (ROC) curve and precision and recall (PR) curve were employed. The performance indicators utilized were the area under the curve (AUC) and PR-AUC. Additionally, the predictive model was evaluated and pathway enrichment scores were generated for each sample by employing methods such as calibration curve, Hosmer-Lemeshow goodness-of-fit test, Brier score, decision curve analysis (DCA), and pathway enrichment analysis using KEGG and Hallmark gene sets. Appropriate statistical methods and visualization tools were utilized to conduct mutation frequency analysis, as well as to compare the differential expression of immune genes and immune cell infiltration between the high and low PS groups.

Results

TNFRSF4 gene prognosis analysis

To investigate the expression of TNFRSF4 in tumors, we conducted a differential expression analysis using the TCGA database. The findings revealed a notable difference in TNFRSF4 expression between tumor and non-tumor samples in HNSCC specimens ($p < 0.001$) (Fig. 2A). We divided the survival analysis of the 475 TCGA HNSCC patients into two groups based on TNFRSF4 expression levels. The TNFRSF4 high expression group ($n = 254$) and the low expression group ($n = 221$) were determined using a cutoff value of 1.6827 (Table I). The high and low expression groups showed no notable variations in the distribution of covariates, including age and gender ($p \geq 0.05$). Nevertheless, notable differences were observed in the allocation of factors such as pathologic stage and histologic grade between the two expression cohorts ($p < 0.05$). In the low expression group, the median survival time was 36.43 months, whereas it was 69.43 months in the high expression group. The Kaplan-Meier curve revealed a statistically significant association between high TNFRSF4 expression and improved overall survival (Fig. 2B).

The analyses revealed that a high level of TNFRSF4 expression was associated with a lower risk of OS in the univariate analysis (HR = 0.589, 95% CI: 0.445–0.781, $p < 0.001$), demonstrating high statistical significance. When performing multivariate analysis and adjusting for other factors, high TNFRSF4 expression (HR = 0.700, 95% CI: 0.516–0.950, $p = 0.022$) demonstrated a protective effect on overall survival, and the association remained statistically significant (Fig. 2C).

During subgroup analysis, within the subgroup without perineural invasion, high TNFRSF4 expression was identified as a protective factor for overall survival, with HR = 0.336, 95% CI: 0.185–0.610, and a highly significant p-value of less than 0.001. However, in the subgroup with perineural invasion of a known or unknown nature, high TNFRSF4 expression did not exhibit a protective effect on overall survival. The p-values for interaction tests were 0.042 and 0.029, indicating a significant interaction between TNFRSF4 expression and the presence of perineural invasion subgroups. In other words, the impact of TNFRSF4 on overall survival differs between these two subgroups based on the presence of perineural invasion (Fig. 2D).

Pathomics prediction of TNFRSF4

We collected a total of 271 samples that included complete pathological images, gene matrices, and clinical information. Using the survminer R package, we determined the cutoff value for the TNFRSF4 gene expression level to be 1.6827. Using this measurement, we classified the individuals into groups with high or low expression levels. Afterwards, we divided the data into two sets, namely a training set and a validation set, using a ratio of 7 to 3. In the training set, we normalized the pathological features, which were extracted using the pyradiomics package, using z-score normalization. Next, we applied the identical mean and standard deviation from the training dataset to standardize the validation dataset. We analyzed the inter-group differences in clinical variables and found that all variables had a p-value greater than 0.05. This indicated that the baseline characteristics of the training set and validation set were similar, ensuring comparability between the two groups (Table II).

Additionally, we applied the mRMR method to select the top 30 features and subsequently used recursive feature elimination (RFE) to identify the final 3 features (Fig. 3A). The mRMR_RFE-selected features were utilized to construct a model using the GBM algorithm in the training set. Figure 3B displays the importance of the selected characteristics in the GBM algorithm.

Evaluation of the model's performance showed that the pathological model demonstrated strong predictive abilities, attaining an AUC score of 0.815 in the training dataset based on the ROC curve and an AUC of 0.726 in the validation dataset. Significantly,the alignment between the predicted probabilities of high gene expression from the pathomics

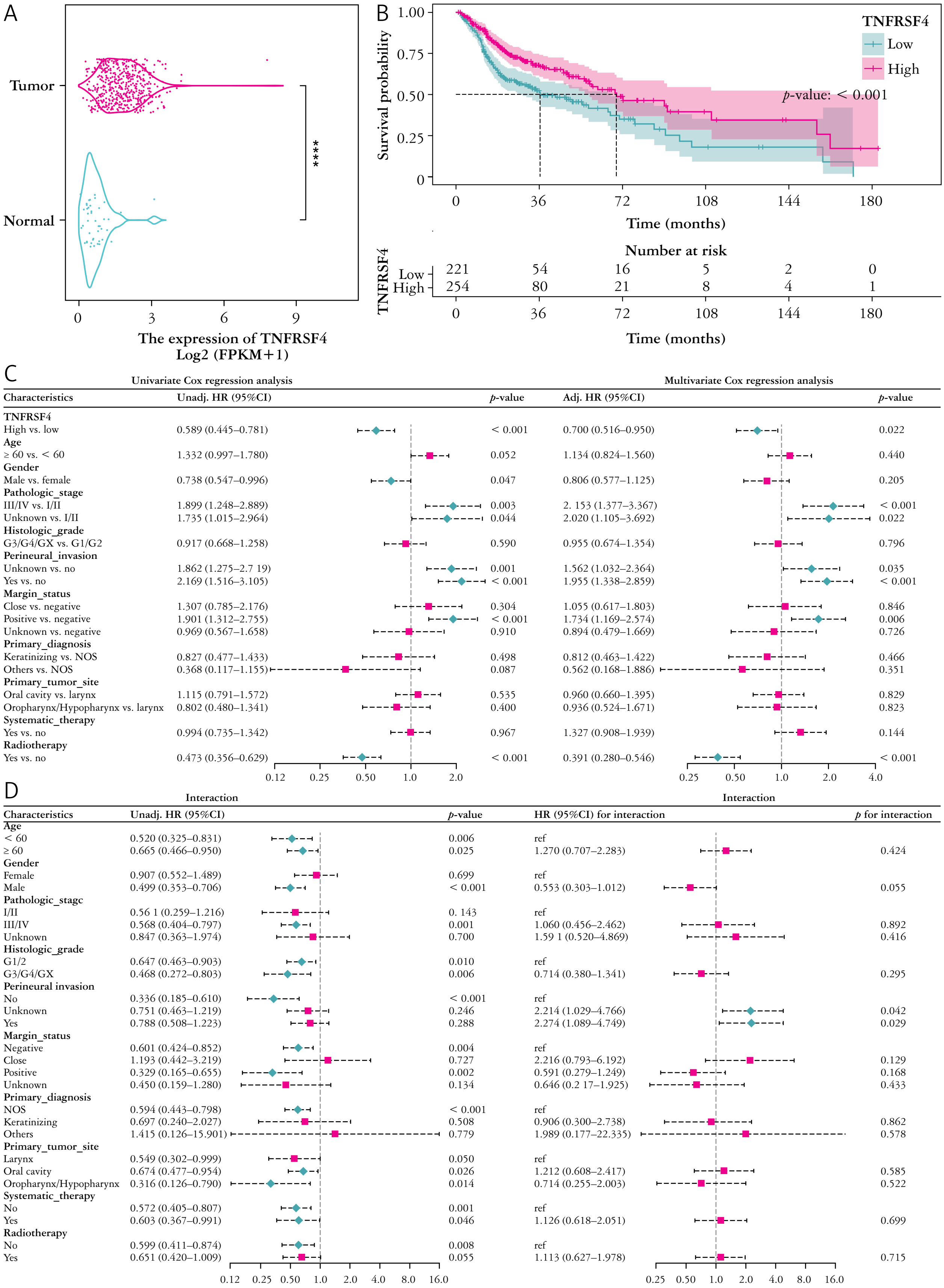

Characteristics	Univariate Cox regression analysis Unadj. HR (95%CI)	*p*-value	Multivariate Cox regression analysis Adj. HR (95%CI)	*p*-value
TNFRSF4				
High vs. low	0.589 (0.445–0.781)	< 0.001	0.700 (0.516–0.950)	0.022
Age				
≥ 60 vs. < 60	1.332 (0.997–1.780)	0.052	1.134 (0.824–1.560)	0.440
Gender				
Male vs. female	0.738 (0.547–0.996)	0.047	0.806 (0.577–1.125)	0.205
Pathologic_stage				
III/IV vs. I/II	1.899 (1.248–2.889)	0.003	2. 153 (1.377–3.367)	< 0.001
Unknown vs. I/II	1.735 (1.015–2.964)	0.044	2.020 (1.105–3.692)	0.022
Histologic_grade				
G3/G4/GX vs. G1/G2	0.917 (0.668–1.258)	0.590	0.955 (0.674–1.354)	0.796
Perineural_invasion				
Unknown vs. no	1.862 (1.275–2.7 19)	0.001	1.562 (1.032–2.364)	0.035
Yes vs. no	2.169 (1.516–3.105)	< 0.001	1.955 (1.338–2.859)	< 0.001
Margin_status				
Close vs. negative	1.307 (0.785–2.176)	0.304	1.055 (0.617–1.803)	0.846
Positive vs. negative	1.901 (1.312–2.755)	< 0.001	1.734 (1.169–2.574)	0.006
Unknown vs. negative	0.969 (0.567–1.658)	0.910	0.894 (0.479–1.669)	0.726
Primary_diagnosis				
Keratinizing vs. NOS	0.827 (0.477–1.433)	0.498	0.812 (0.463–1.422)	0.466
Others vs. NOS	0.368 (0.117–1.155)	0.087	0.562 (0.168–1.886)	0.351
Primary_tumor_site				
Oral cavity vs. larynx	1.115 (0.791–1.572)	0.535	0.960 (0.660–1.395)	0.829
Oropharynx/Hypopharynx vs. larynx	0.802 (0.480–1.341)	0.400	0.936 (0.524–1.671)	0.823
Systematic_therapy				
Yes vs. no	0.994 (0.735–1.342)	0.967	1.327 (0.908–1.939)	0.144
Radiotherapy				
Yes vs. no	0.473 (0.356–0.629)	< 0.001	0.391 (0.280–0.546)	< 0.001

Characteristics	Interaction Unadj. HR (95%CI)	*p*-value	Interaction HR (95%CI) for interaction	*p* for interaction
Age				
< 60	0.520 (0.325–0.831)	0.006	ref	
≥ 60	0.665 (0.466–0.950)	0.025	1.270 (0.707–2.283)	0.424
Gender				
Female	0.907 (0.552–1.489)	0.699	ref	
Male	0.499 (0.353–0.706)	< 0.001	0.553 (0.303–1.012)	0.055
Pathologic_stagc				
I/II	0.56 1 (0.259–1.216)	0. 143	ref	
III/IV	0.568 (0.404–0.797)	0.001	1.060 (0.456–2.462)	0.892
Unknown	0.847 (0.363–1.974)	0.700	1.59 1 (0.520–4.869)	0.416
Histologic_grade				
G1/2	0.647 (0.463–0.903)	0.010	ref	
G3/G4/GX	0.468 (0.272–0.803)	0.006	0.714 (0.380–1.341)	0.295
Perineural invasion				
No	0.336 (0.185–0.610)	< 0.001	ref	
Unknown	0.751 (0.463–1.219)	0.246	2.214 (1.029–4.766)	0.042
Yes	0.788 (0.508–1.223)	0.288	2.274 (1.089–4.749)	0.029
Margin_status				
Negative	0.601 (0.424–0.852)	0.004	ref	
Close	1.193 (0.442–3.219)	0.727	2.216 (0.793–6.192)	0.129
Positive	0.329 (0.165–0.655)	0.002	0.591 (0.279–1.249)	0.168
Unknown	0.450 (0.159–1.280)	0.134	0.646 (0.2 17–1.925)	0.433
Primary_diagnosis				
NOS	0.594 (0.443–0.798)	< 0.001	ref	
Keratinizing	0.697 (0.240–2.027)	0.508	0.906 (0.300–2.738)	0.862
Others	1.415 (0.126–15.901)	0.779	1.989 (0.177–22.335)	0.578
Primary_tumor_site				
Larynx	0.549 (0.302–0.999)	0.050	ref	
Oral cavity	0.674 (0.477–0.954)	0.026	1.212 (0.608–2.417)	0.585
Oropharynx/Hypopharynx	0.316 (0.126–0.790)	0.014	0.714 (0.255–2.003)	0.522
Systematic_therapy				
No	0.572 (0.405–0.807)	0.001	ref	
Yes	0.603 (0.367–0.991)	0.046	1.126 (0.618–2.051)	0.699
Radiotherapy				
No	0.599 (0.411–0.874)	0.008	ref	
Yes	0.651 (0.420–1.009)	0.055	1.113 (0.627–1.978)	0.715

Fig. 2. Expression and prognostic analysis of TNFRSF4 in head and neck squamous cell carcinoma (HNSCC). **A)** The expression of TNFRSF4 between the tumor and non-tumor groups in HNSCC. **B)** The Kaplan-Meier curve indicates a statistically significant association between high expression of TNFRSF4 and improved OS. **C)** The relationship between high and low expression of the TNFRSF4 molecule and the occurrence of survival outcomes with various clinical characteristics was assessed through single-factor and multi-factor analyses using the Cox proportional hazards model. **D)** Univariate Cox regression was utilized for exploratory subgroup analysis to explore the impact of TNFRSF4 on patient prognosis in various subgroups of each covariate. Furthermore, the likelihood ratio test was employed to assess the interaction between TNFRSF4 expression and other covariates

Table I. Correlation between TNFRSF4 expression and clinicopathologic characteristics in 475 head and neck squamous cell carcinoma (HNSCC) cases

VARIABLES	TOTAL (*N* = 475)	LOW (*N* = 221)	HIGH (*N* = 254)	*P*
Age, *n* (%)				
<60	207 (44)	94 (43)	113 (44)	0.737
≥ 60	268 (56)	127 (57)	141 (56)	
Gender, *n* (%)				
Female	126 (27)	56 (25)	70 (28)	0.658
Male	349 (73)	165 (75)	184 (72)	
Pathologic stage, *n* (%)				
I/II	90 (19)	34 (15)	56 (22)	0.003
III/IV	320 (67)	166 (75)	154 (61)	
Unknown	65 (14)	21 (10)	44 (17)	
Histologic grade, *n* (%)				
G1/G2	346 (73)	175 (79)	171 (67)	0.005
G3/G4/GX	129 (27)	46 (21)	83 (33)	
Perineural invasion, *n* (%)				
No	180 (38)	74 (33)	106 (42)	0.085
Unknown	139 (29)	64 (29)	75 (30)	
Yes	156 (33)	83 (38)	73 (29)	
Margin status, *n* (%)				
Close	44 (9)	21 (10)	23 (9)	0.977
Negative	326 (69)	153 (69)	173 (68)	
Positive	55 (12)	25 (11)	30 (12)	
Unknown	50 (11)	22 (10)	28 (11)	
Primary diagnosis, *n* (%)				
Keratinizing	51 (11)	22 (10)	29 (11)	0.481
NOS	404 (85)	192 (87)	212 (83)	
Others	20 (4)	7 (3)	13 (5)	
Primary tumor site, *n* (%)				
Larynx	105 (22)	49 (22)	56 (22)	0.01
Oral cavity	293 (62)	148 (67)	145 (57)	
Oropharynx/Hypopharynx	77 (16)	24 (11)	53 (21)	
Systematic therapy, *n* (%)				
No	313 (66)	147 (67)	166 (65)	0.866
Yes	162 (34)	74 (33)	88 (35)	
Radiotherapy, *n* (%)				
No	219 (46)	115 (52)	104 (41)	0.02
Yes	256 (54)	106 (48)	150 (59)	

model and the actual values was indicated by the calibration curve and the Hosmer-Lemeshow goodness-of-fit test ($p > 0.05$). Furthermore, the DCA underscored the model's substantial clinical utility (Fig. 3C-H).

The pathomics score (PS), which represents the pathological histology score, was computed for the overlapping samples using a pathological histology model. The Wilcoxon test was used to compare the distribution of PS between the high and low gene expression groups. The results showed that in both

Table II. Analysis of inter-group differences between training and validation sets

Variables	Total (*N* = 271)	Train (*n* = 191)	Validation (*n* = 80)	*p*
TNFRSF4, *n* (%)				
Low	128 (47)	90 (47)	38 (48)	1
High	143 (53)	101 (53)	42 (52)	
Age, *n* (%)				
< 60	111 (41)	75 (39)	36 (45)	0.459
≥ 60	160 (59)	116 (61)	44 (55)	
Gender, *n* (%)				
Female	75 (28)	52 (27)	23 (29)	0.915
Male	196 (72)	139 (73)	57 (71)	
Pathologic stage, *n* (%)				
I/II	52 (19)	40 (21)	12 (15)	0.258
III/IV	191 (70)	129 (68)	62 (78)	
Unknown	28 (10)	22 (12)	6 (8)	
Histologic grade, *n* (%)				
G1/G2	204 (75)	141 (74)	63 (79)	0.482
G3/G4/GX	67 (25)	50 (26)	17 (21)	
Perineural invasion, *n* (%)				
No	106 (39)	74 (39)	32 (40)	0.19
Unknown	66 (24)	52 (27)	14 (18)	
Yes	99 (37)	65 (34)	34 (42)	
Margin status, *n* (%)				
Close	36 (13)	26 (14)	10 (12)	0.365
Negative	173 (64)	122 (64)	51 (64)	
Positive	39 (14)	24 (13)	15 (19)	
Unknown	23 (8)	19 (10)	4 (5)	
Primary diagnosis, *n* (%)				
Keratinizing	32 (12)	18 (9)	14 (18)	0.104
NOS	230 (85)	165 (86)	65 (81)	
Others	9 (3)	8 (4)	1 (1)	
Primary tumor site, *n* (%)				
Larynx	67 (25)	48 (25)	19 (24)	0.476
Oral cavity	171 (63)	117 (61)	54 (68)	
Oropharynx/Hypopharynx	33 (12)	26 (14)	7 (9)	
Systematic therapy, *n* (%)				
No	189 (70)	138 (72)	51 (64)	0.213
Yes	82 (30)	53 (28)	29 (36)	
Radiotherapy, *n* (%)				
No	132 (49)	97 (51)	35 (44)	0.356
Yes	139 (51)	94 (49)	45 (56)	
Overall survival, *n* (%)				
Alive	150 (55)	105 (55)	45 (56)	0.953
Dead	121 (45)	86 (45)	35 (44)	
Survival time, median (Q1, Q3)	22.1 (12.83, 44.47)	22.63 (12.87, 44.55)	21.4 (12.77, 44.05)	0.995

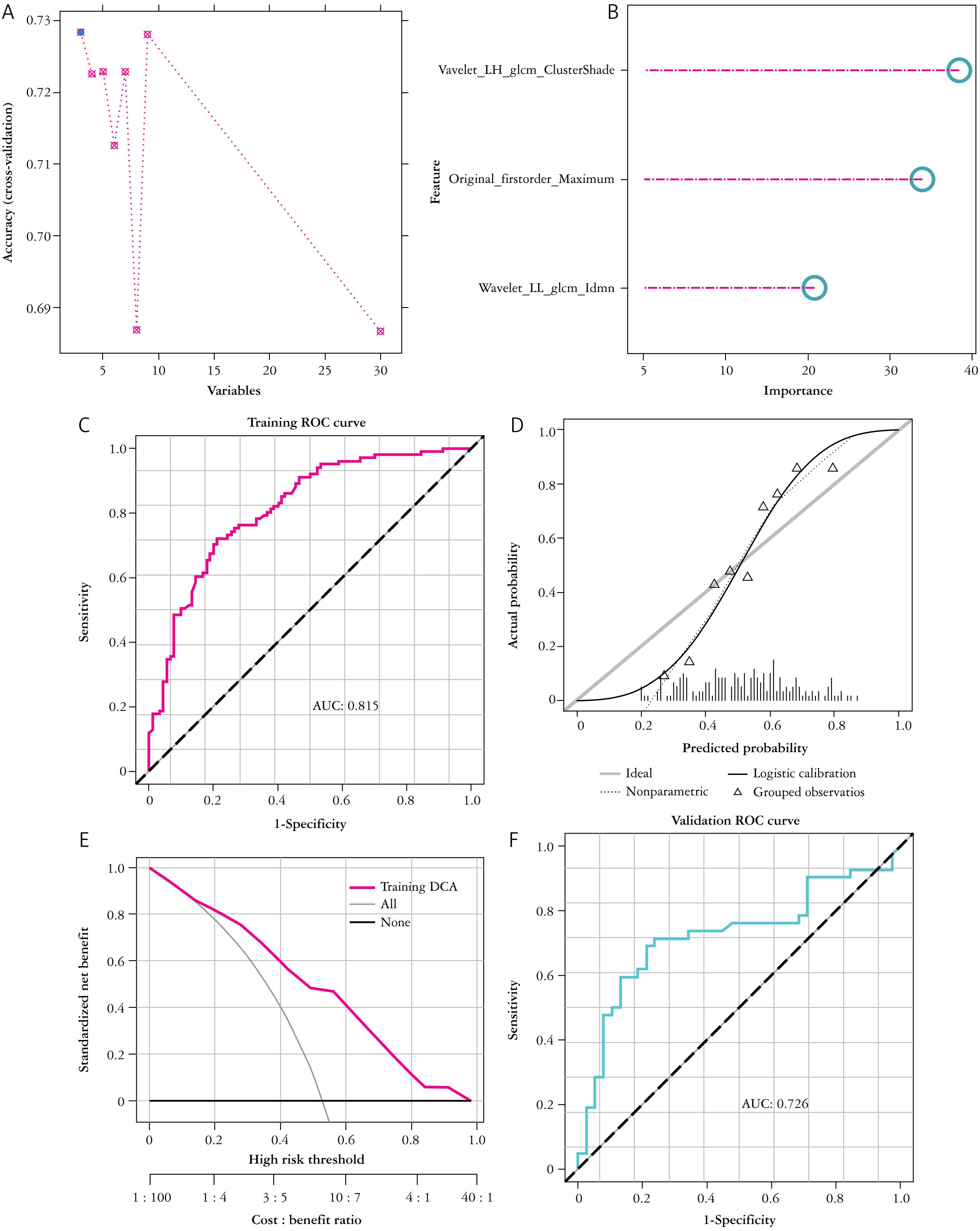

Fig. 3. Establishment and validation of the machine learning model. **A**) After applying the mRMR method, the top 30 features were chosen from the pre-pathological tissue images, and subsequently subjected to feature selection using the RFE technique, resulting in the identification of 3 final features. **B**) The importance of the selected features was evaluated using the GBM algorithm. **C, F**) The ROC curves of the training and validation sets were generated

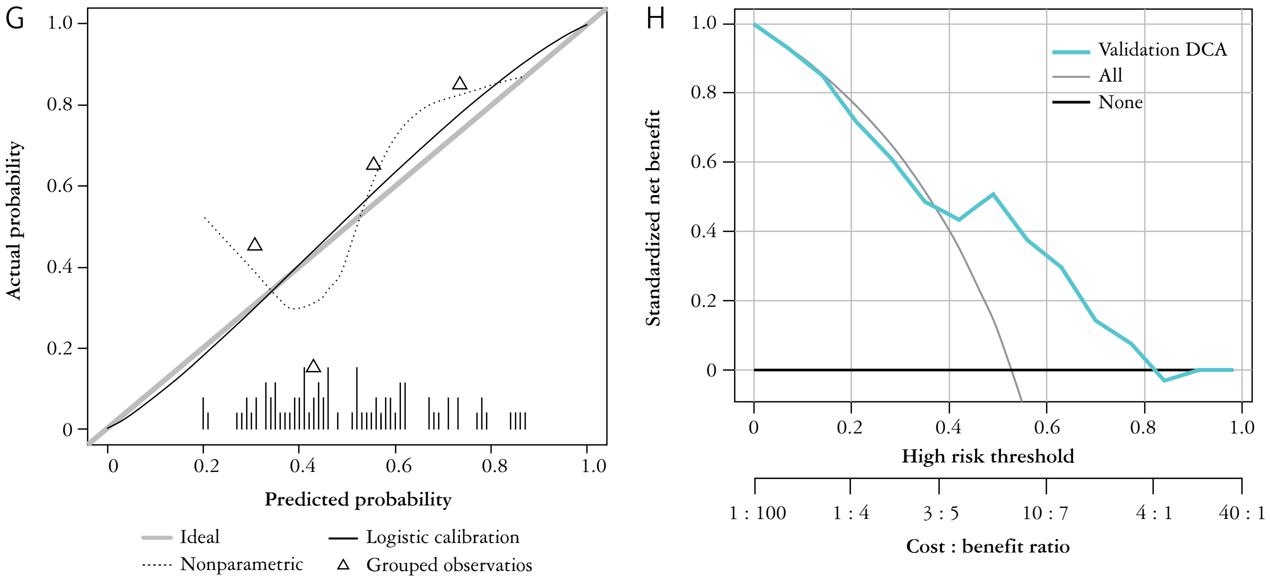

Fig. 3. Cont. **D, G**) The calibration curve demonstrates the high consistency of the predictive model of pathological genomics between the estimated probability of high gene expression and the actual values. **E, H**) The DCA illustrates the model's high clinical utility

the training and validation datasets, the TNFRSF4 high-expressing group displayed notably elevated PS values in comparison to the low-expressing group (Fig. 4A,B). Subsequently, integrating the pathological histology score with clinical data, we determined the cutoff value of PS using the survminer package. This allowed us to classify PS as a binary variable (low/high). With this low and high classification of PS, we constructed a table (Table III) to present the baseline data of various clinical variables.

According to the Kaplan-Meier curve, high PS values were significantly correlated with improved overall survival, with $p = 0.01$ (Fig. 4C). The high PS group had a median survival time of 68.8 months, whereas the low PS group had lower median survival of 48.87 months. Statistical significance was demonstrated in the univariate analysis, where high PS expression was found to be a protective factor for OS (HR = 0.626, 95% CI: 0.437–0.898, $p = 0.011$). Furthermore, a significant protective effect on overall survival was observed in the multivariate analysis after adjusting for various factors, with a high PS value (HR = 0.600, 95% CI: 0.412–0.874, $p = 0.008$) demonstrating statistical significance (Fig. 5A). Notably, the subgroup analysis outcomes, illustrated in the figure, revealed no significant interaction between PS and most clinical variables in the subgroups (Fig. 5B).

Analysis of possible mechanism of TNFRSF4 pathomics

We performed a differential expression analysis of genes (DEGs) to examine the enrichment of the PS high/low groups in HNSCC. The results revealed a notable enhancement of signaling pathways such as leukocyte transendothelial migration in the KEGG gene collections for the low PS group (Fig. 6A). Conversely, in a Hallmark gene set analysis, the high PS group exhibited significant enrichment in signaling pathways such as oxidative phosphorylation (OXPHOS) (Fig. 6B).

Additionally, we conducted an immunological analysis by exploring the differential expression of immunological genes between the low and high PS groups. The examination uncovered a noteworthy increase in the expression of genes such as NRP1 and IDO1 in the group with high PS expression ($p < 0.01$) (Fig. 6C). Furthermore, the analysis of immune cell infiltration in the high and low PS expression groups revealed a significant increase in the presence of CD8 T cells, CD4 memory activated T cells, follicular helper T cells, and M1 macrophages in the high PS group ($p < 0.001$) (Fig. 6D).

Furthermore, we assessed the relationship between the somatic mutation data and the model prediction of PS grouping in TCGA-HNSCC patients. The analysis revealed that missense mutation was the most common type, followed by nonsense mutation. The TP53 gene exhibited a mutation rate of over 70% in both the high and low PS groups. Furthermore, the high PS cohort exhibited an elevated mutation frequency in genes such as TTN, FAT1, and CDKN2A in comparison to the low PS cohort (Fig. 6E,F).

Discussion

In this study, we conducted an analysis on histopathological image features (HIF) and employed machine learning algorithms to identify relevant features. The objective was to build a model utiliz-

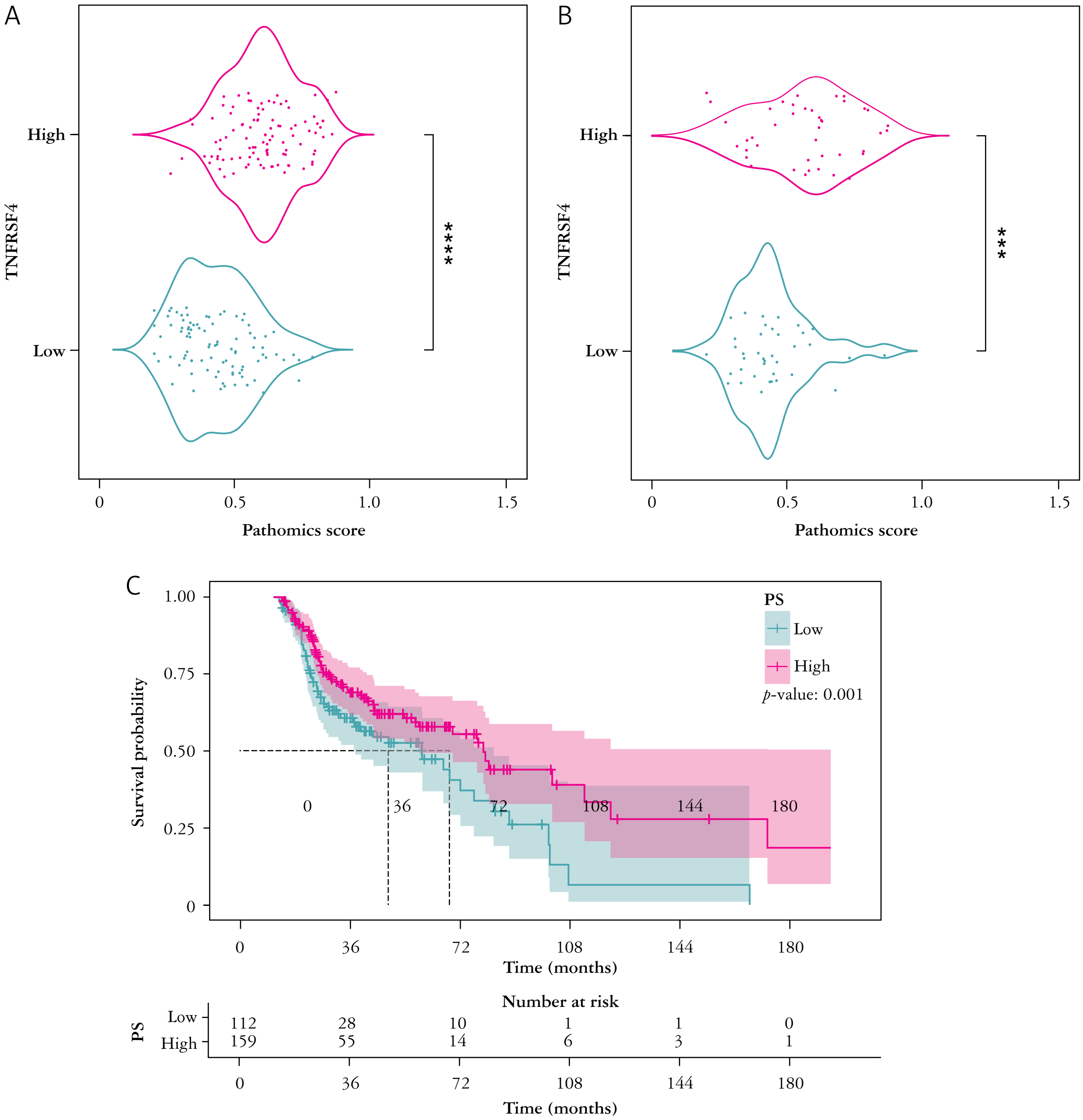

Fig. 4. The Wilcoxon test was employed to compare the distribution difference of PS between high and low gene expression groups. In both the training set (**A**) and validation set (**B**), higher PS values were observed in the TNFRSF4 molecule high expression group compared to the low expression group. **C**) The Kaplan-Meier curve revealed a significant association between high PS and improved overall survival ($p = 0.01$)

ing clinical data that could forecast the expression of the *TNFRSF4* gene as well as the prognosis of patients with HNSCC. Using pathomics, our research is a pioneering investigation to examine the expression of *TNFRSF4* in patients with HNSCC. The examination of *TNFRSF4* expression levels in tumor tissue indicated that this gene functions as a separate prognostic determinant for HNSCC. By observing the differences in pathological features between cases of high and low *TNFRSF4* expression in HNSCC, we successfully developed a relevant and effective pathological histology prediction model. In the training set, the model's ROC curves demonstrated significant predictive capability, achieving an AUC value of 0.815, while in the validation set, the AUC value was 0.726. Furthermore, the PS displayed a significant correlation with the improvement of overall survival in HNSCC patients ($p = 0.01$). Our prognostic model, built on HIF, is believed to provide better predictive accuracy and efficiency than other omics methods such as genomics, transcriptomics, and proteomics. The DCA also showed that our model based

Table III. Correlation between PS and clinicopathologic characteristics in 271 head and neck squamous cell carcinoma (HNSCC) cases

Variables	Total (N = 271)	Low (n = 112)	High (n = 159)	p
Age, *n* (%)				
< 60	111 (41)	43 (38)	68 (43)	0.551
≥ 60	160 (59)	69 (62)	91 (57)	
Gender, *n* (%)				
Female	75 (28)	33 (29)	42 (26)	0.678
Male	196 (72)	79 (71)	117 (74)	
Pathologic stage, *n* (%)				
I/II	52 (19)	22 (20)	30 (19)	0.584
III/IV	191 (70)	76 (68)	115 (72)	
Unknown	28 (10)	14 (12)	14 (9)	
Histologic grade, *n* (%)				
G1/G2	204 (75)	84 (75)	120 (75)	1
G3/G4/GX	67 (25)	28 (25)	39 (25)	
Perineural invasion, *n* (%)				
No	106 (39)	44 (39)	62 (39)	0.471
Unknown	66 (24)	31 (28)	35 (22)	
Yes	99 (37)	37 (33)	62 (39)	
Margin status, *n* (%)				
Negative	173 (64)	66 (59)	107 (67)	0.437
Close	36 (13)	15 (13)	21 (13)	
Positive	39 (14)	19 (17)	20 (13)	
Unknown	23 (8)	12 (11)	11 (7)	
Primary diagnosis, *n* (%)				
NOS	230 (85)	97 (87)	133 (84)	0.566
Keratinizing	32 (12)	13 (12)	19 (12)	
Others	9 (3)	2 (2)	7 (4)	
Primary tumor site, *n* (%)				
Larynx	67 (25)	32 (29)	35 (22)	0.353
Oral cavity	171 (63)	69 (62)	102 (64)	
Oropharynx/Hypopharynx	33 (12)	11 (10)	22 (14)	
Systematic therapy, *n* (%)				
No	189 (70)	83 (74)	106 (67)	0.239
Yes	82 (30)	29 (26)	53 (33)	
Radiotherapy, *n* (%)				
No	132 (49)	61 (54)	71 (45)	0.142
Yes	139 (51)	51 (46)	88 (55)	

on pathological histology has great clinical usefulness and can aid in personalized cancer patient care.

Worldwide, more than 650,000 cases of HNSCC are detected annually [2], commonly appearing in later stages with the invasion of nearby tissues and the spread of cancer cells to lymph nodes. More than 50% of patients experience relapse within three years [3]. The majority of individuals with HNSCC exhibit reduced absolute lymphocyte levels compared to healthy individuals. Additionally, they experience compromised function of natural killer cells and antigen presentation, indicating a correlation between

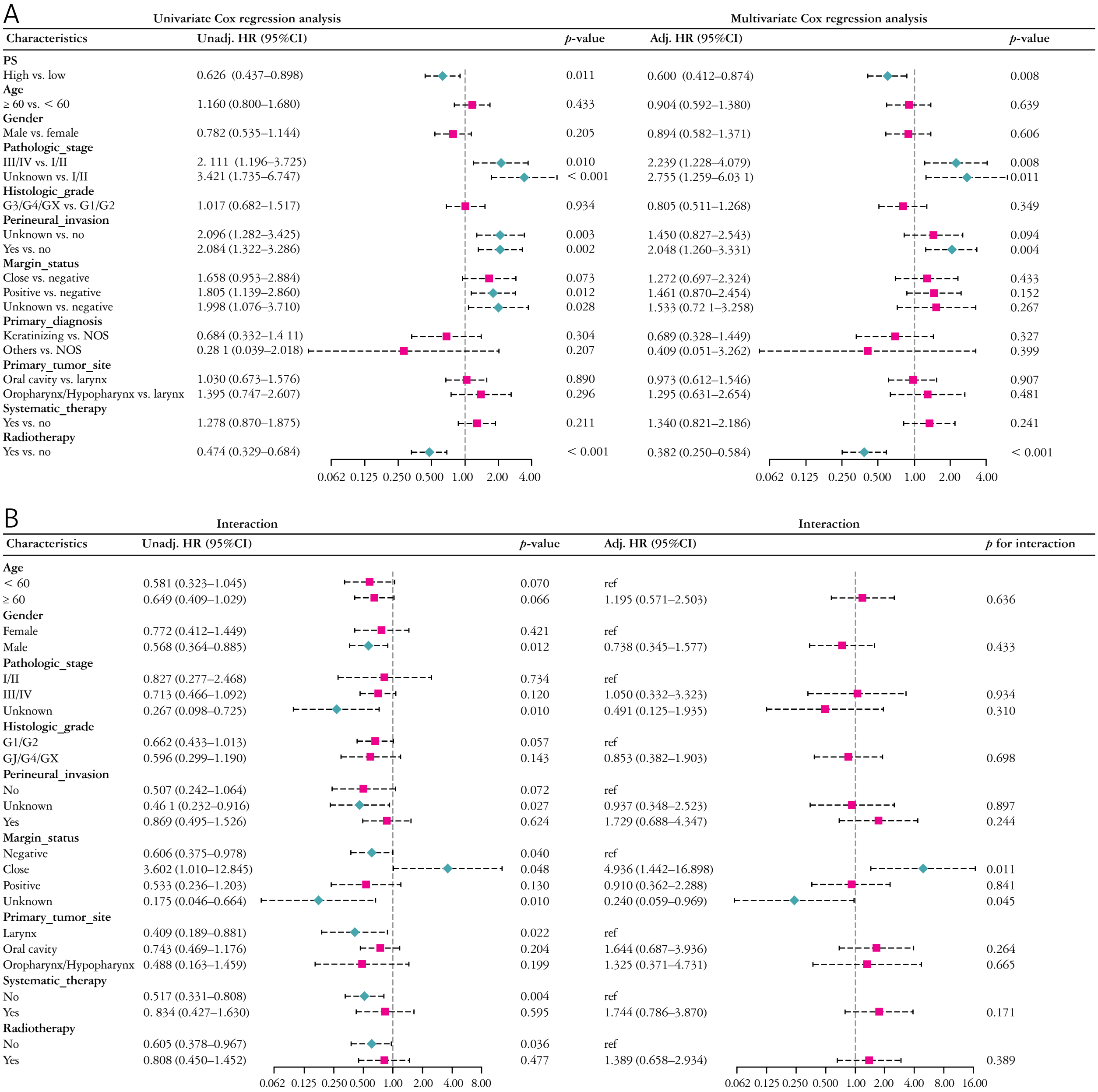

	Univariate Cox regression analysis		Multivariate Cox regression analysis	
Characteristics	**Unadj. HR (95%CI)**	***p*-value**	**Adj. HR (95%CI)**	***p*-value**
PS				
High vs. low	0.626 (0.437–0.898)	0.011	0.600 (0.412–0.874)	0.008
Age				
≥ 60 vs. < 60	1.160 (0.800–1.680)	0.433	0.904 (0.592–1.380)	0.639
Gender				
Male vs. female	0.782 (0.535–1.144)	0.205	0.894 (0.582–1.371)	0.606
Pathologic_stage				
III/IV vs. I/II	2. 111 (1.196–3.725)	0.010	2.239 (1.228–4.079)	0.008
Unknown vs. I/II	3.421 (1.735–6.747)	< 0.001	2.755 (1.259–6.03 1)	0.011
Histologic_grade				
G3/G4/GX vs. G1/G2	1.017 (0.682–1.517)	0.934	0.805 (0.511–1.268)	0.349
Perineural_invasion				
Unknown vs. no	2.096 (1.282–3.425)	0.003	1.450 (0.827–2.543)	0.094
Yes vs. no	2.084 (1.322–3.286)	0.002	2.048 (1.260–3.331)	0.004
Margin_status				
Close vs. negative	1.658 (0.953–2.884)	0.073	1.272 (0.697–2.324)	0.433
Positive vs. negative	1.805 (1.139–2.860)	0.012	1.461 (0.870–2.454)	0.152
Unknown vs. negative	1.998 (1.076–3.710)	0.028	1.533 (0.72 1–3.258)	0.267
Primary_diagnosis				
Keratinizing vs. NOS	0.684 (0.332–1.4 11)	0.304	0.689 (0.328–1.449)	0.327
Others vs. NOS	0.28 1 (0.039–2.018)	0.207	0.409 (0.051–3.262)	0.399
Primary_tumor_site				
Oral cavity vs. larynx	1.030 (0.673–1.576)	0.890	0.973 (0.612–1.546)	0.907
Oropharynx/Hypopharynx vs. larynx	1.395 (0.747–2.607)	0.296	1.295 (0.631–2.654)	0.481
Systematic_therapy				
Yes vs. no	1.278 (0.870–1.875)	0.211	1.340 (0.821–2.186)	0.241
Radiotherapy				
Yes vs. no	0.474 (0.329–0.684)	< 0.001	0.382 (0.250–0.584)	< 0.001

	Interaction		Interaction	
Characteristics	**Unadj. HR (95%CI)**	***p*-value**	**Adj. HR (95%CI)**	***p* for interaction**
Age				
< 60	0.581 (0.323–1.045)	0.070	ref	
≥ 60	0.649 (0.409–1.029)	0.066	1.195 (0.571–2.503)	0.636
Gender				
Female	0.772 (0.412–1.449)	0.421	ref	
Male	0.568 (0.364–0.885)	0.012	0.738 (0.345–1.577)	0.433
Pathologic_stage				
I/II	0.827 (0.277–2.468)	0.734	ref	
III/IV	0.713 (0.466–1.092)	0.120	1.050 (0.332–3.323)	0.934
Unknown	0.267 (0.098–0.725)	0.010	0.491 (0.125–1.935)	0.310
Histologic_grade				
G1/G2	0.662 (0.433–1.013)	0.057	ref	
GJ/G4/GX	0.596 (0.299–1.190)	0.143	0.853 (0.382–1.903)	0.698
Perineural_invasion				
No	0.507 (0.242–1.064)	0.072	ref	
Unknown	0.46 1 (0.232–0.916)	0.027	0.937 (0.348–2.523)	0.897
Yes	0.869 (0.495–1.526)	0.624	1.729 (0.688–4.347)	0.244
Margin_status				
Negative	0.606 (0.375–0.978)	0.040	ref	
Close	3.602 (1.010–12.845)	0.048	4.936 (1.442–16.898)	0.011
Positive	0.533 (0.236–1.203)	0.130	0.910 (0.362–2.288)	0.841
Unknown	0.175 (0.046–0.664)	0.010	0.240 (0.059–0.969)	0.045
Primary_tumor_site				
Larynx	0.409 (0.189–0.881)	0.022	ref	
Oral cavity	0.743 (0.469–1.176)	0.204	1.644 (0.687–3.936)	0.264
Oropharynx/Hypopharynx	0.488 (0.163–1.459)	0.199	1.325 (0.371–4.731)	0.665
Systematic_therapy				
No	0.517 (0.331–0.808)	0.004	ref	
Yes	0. 834 (0.427–1.630)	0.595	1.744 (0.786–3.870)	0.171
Radiotherapy				
No	0.605 (0.378–0.967)	0.036	ref	
Yes	0.808 (0.450–1.452)	0.477	1.389 (0.658–2.934)	0.389

Fig. 5. Analysis of the relationship between PS and clinical characteristics in head and neck squamous cell carcinoma. **A**) Using the Cox proportional hazards model, both univariate and multivariate analyses were conducted to examine the association between the high and low PS groups and different clinical features with respect to survival outcomes. **B**) Exploratory subgroup analysis was conducted using univariate Cox regression to assess the influence of PS values on patient prognosis within various subgroups of each covariate. Furthermore, the likelihood ratio test was employed to evaluate the interaction between the expression of PS values and other covariates

immune suppression and the onset and progression of HNSCC [12, 13]. Research has indicated that immune-suppressing cells, such as regulatory T cells (Tregs), are mobilized and stimulated within the tumor location [14]. Furthermore, these cells are abundant in the bloodstream of individuals with tumors [15], resulting in the development of a tumor microenvironment (TME) that hampers the immune system. TNFRSF4, along with its ligand, contributes to the stimulation of T cell clonal expansion, memory T cell production and maintenance [16–18], augmentation of low-effector T cell function [19], inhibition of immune tolerance formation, and disruption of established immune tolerance [20]. Studies on squamous cell carcinoma of the skin have shown that the quantity of regulatory T cells (Tregs) surpasses that of effector T cells significantly, with tumor Tregs predominantly expressing TNFRSF4. Stimulation of TNFRSF4 on tumor Tregs can hinder their immunosuppressive impact, enhance the growth of tumor CD4+ T cells, and demonstrate anti-tumor properties [21]. Diverse cancer types, such as breast cancer, melanoma, lymphoma,

]

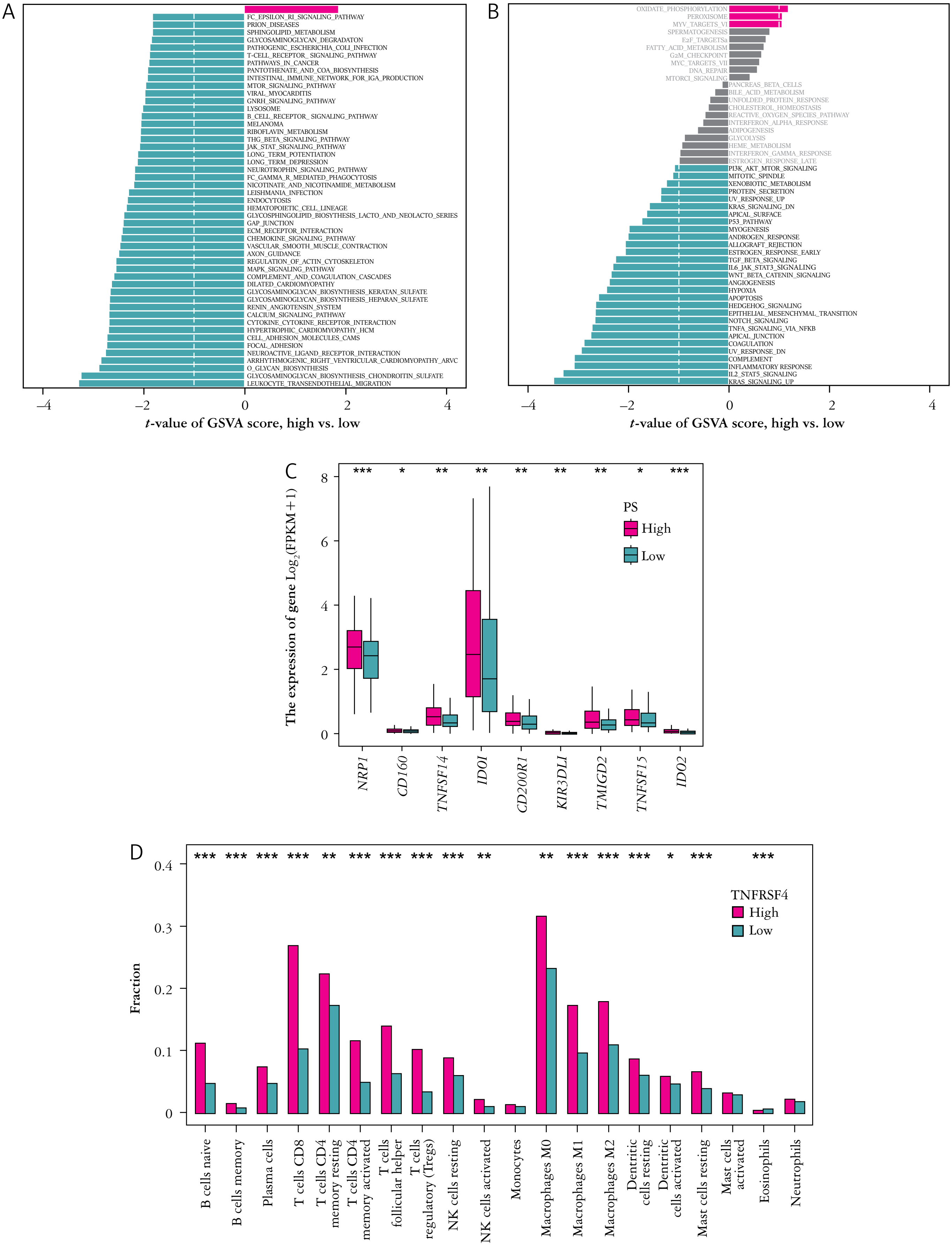

Fig. 6. Possible mechanism analysis of TNFRSF4 pathomics. **A**) The pathway enrich score of KEGG pathway gene sets in all samples. **B**) The pathway enrich score of Hallmark pathway gene sets in all samples. **C**) Differential expression analysis of immune genes between high and low PS groups. **D**) Differential analysis of immune cell abundance between high and low PS groups

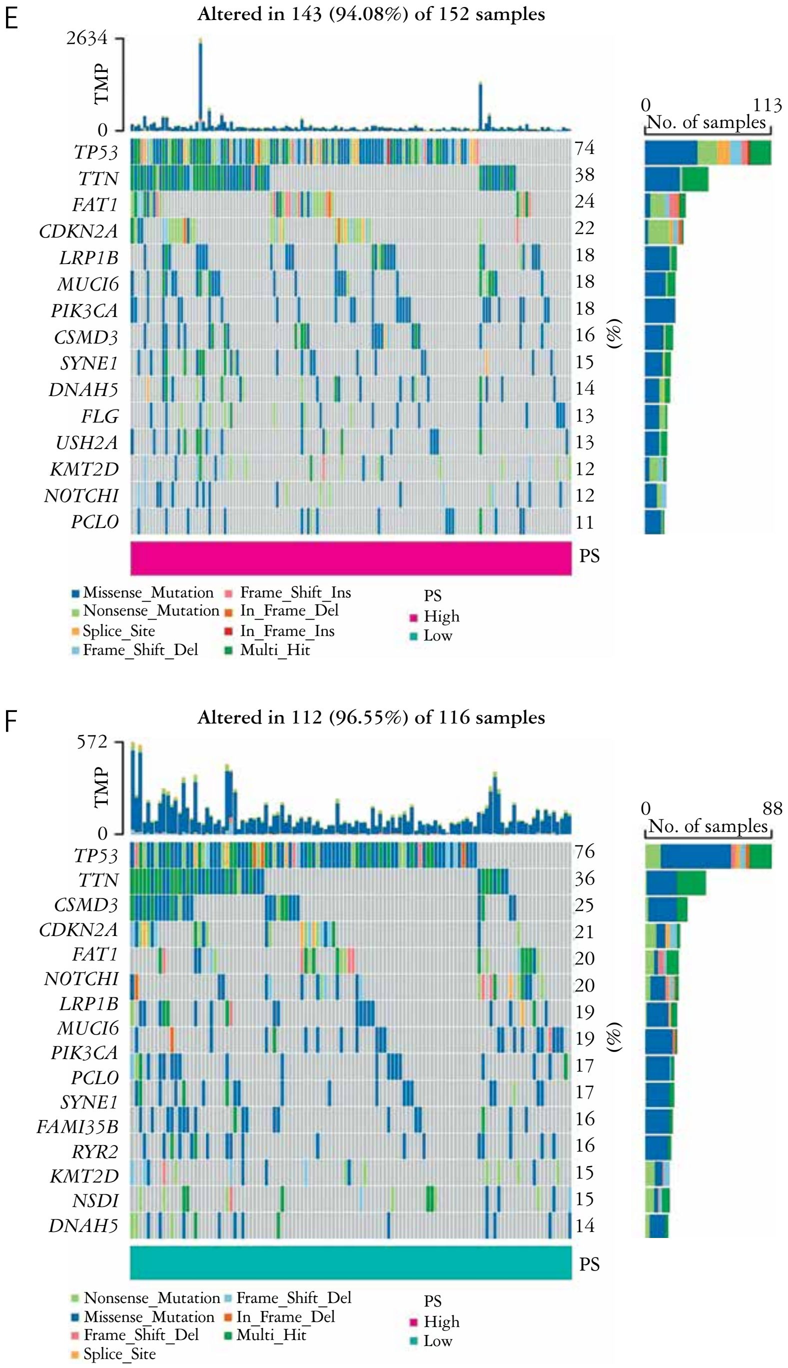

Fig. 6. Cont. **E**) Gene mutation analysis was performed in the high PS group. **F**) Gene mutation analysis was conducted in the low PS group

and colorectal cancer [7, 8, 22, 23], have shown similar outcomes. Nevertheless, TNFRSF4 presents conflicting characteristics, mainly because its prognostic influence varies among different tumor types. The inconsistent findings can be accounted for by the diverse control of TME and Tregs [24]. In the case of HNSCC, we observed that the levels of TNFRSF4 expression in tumor tissue were a significant prognostic indicator (HR = 0.589, 95% CI: 0.445–0.781, $p < 0.001$), and elevated TNFRSF4 expression levels frequently indicated a more favorable prognosis. Furthermore, there are ongoing investigations into combination immune therapy trials that focus on TNFRSF4 in different types of tumors. The objective is to attain enhanced anti-tumor immune responses in solid tumors that have recurred or metastasized [5]. This indicates the potential for TNFRSF4 in the treatment of HNSCC tumor cells and their surrounding microenvironment.

The examination of tissue samples is crucial in determining and classifying tumors, providing vital direction for individualized therapy. Pathologists have traditionally relied on optical microscopes to examine tissue slides for diagnostic purposes. However, the emergence of digital pathology (DP) and its integration with artificial intelligence (AI) has given rise to computational pathology, opening new avenues for research in the field of oncology. The advent of high-definition whole-slide imaging (WSIs) has opened up opportunities for computational pathology and computer-aided diagnosis. Unlike costly molecular biology detection methods, studies have revealed that varying levels of molecular expression can result in morphological changes in cells. AI, utilizing deep learning, successfully distinguished between lung squamous cell carcinoma (LUSC) and lung adenocarcinoma (LUAD) (AUC = 0.950). Additionally, it predicted common molecular changes including STK11, EGFR, FAT1, SETBP1, KRAS, and TP53 (AUCs ranging from 0.733 to 0.856) [25]. Kim *et al.* [26] constructed a sophisticated deep learning algorithm utilizing a dataset of 257 instances of melanoma, enabling the automatic detection of regions abundant in tumors (with an AUC score of 0.98). Furthermore, the model successfully predicted the existence of BRAF or NRAS mutations with AUC scores of 0.83 and 0.92, respectively. Similar results have been recorded in research studies on prostate adenocarcinoma [27], thyroid tumors [28], and gastrointestinal tumors [29, 30]. The study's findings emphasize the effectiveness of computerized techniques in precisely capturing anatomical structures and overall patterns observed in tissue sections. Efficiently characterizing and systematically incorporating these identifiable traits can help determine the expression of the *TNFRSF4* gene and predict the survival prognosis of patients with HNSCC. This significant correlation between the morphological attributes and their underlying biological characteristics substantiates the predictive potential of these identified markers.

The TNM staging system is presently the most commonly utilized index for tumor staging, being employed to evaluate the prognosis and provide treatment guidance for different types of cancer [31, 32]. Nevertheless, the evaluation of TNM staging is primarily reliant on the tumor's macroscopic features. Recent studies, however, have indicated that the microscopic features of tissue slides are also key factors in tailored tumor treatment [11, 33, 34]. Therefore, our study asserts that the amalgamation of pathological and clinical factors is critical in assisting clinicians in prognostication, visualization and assessing critical factors, guiding individualized tumor treatment.

Our study selected 10 sub-images from the histopathological images of each HNSCC patient and subjected them to image standardization, extracting a total of 465 tissue morphological features. To identify the optimal subset of features, the mRMR and RFE algorithms were utilized. The mRMR method pinpointed the top 30 features, which were further refined through RFE feature selection. These algorithms not only considered the correlation between features and the variables to be predicted but also took into account the correlation between the features themselves, resulting in more accurate results. The results of our study suggest that the variations in the texture and structure of histopathological images can accurately demonstrate the presence of particular molecules such as TNFRSF4 and forecast the prognosis of patients. Identifying these numerical image characteristics manually can be difficult, but machine deep learning techniques can efficiently detect them. Moreover, our analyses using both univariate and multivariate Cox models revealed the considerable predictive significance of image characteristics in relation to overall survival. Histopathological images can be objectively and quantitatively measured using a variety of features, such as Zernike shape features and granularity, which serve as a standard for measurement. In line with our investigation, previous studies have also shown a correlation between survival results in the HNSCC community and morphological formations at the cellular scale (such as size and form), along with the general pixel characteristics of visuals (such as pattern and brightness) [9-11]. Hence, histopathological images have potential practical value in analyzing the expression of specific molecules, such as TNFRSF4, and concurrently predicting the survival of HNSCC patients.

Numerous studies have demonstrated the significant correlation between histopathological images and molecular and genetic data [30, 35-38]. Due to the high tumor heterogeneity, quantitative descriptions of pathological and imaging phenotypes can complement the limitations of more microscopic molecular or genetic detection and observation methods. Huang *et al.* [39] investigated the relationship among gene expression, genetic variation, clinical data, methylation, and digital pathology images in 33 types of cancer, uncovering the correlation between these datasets. To investigate the potential biological role of TNFRSF4 in HNSCC, we conducted pathway enrichment analyses using KEGG and Hallmark, combining immune gene differential analysis and immune cell abundance analysis. The findings suggested that TNFRSF4 is deeply involved in HNSCC's immune behavior. The Hallmark gene set's PS high-scoring group demonstrated significant enrichment in oxidative phosphorylation pathways. In their study of HNSCC, Poropatich *et al.* [40] discovered that TNFRSF4+ plasmacytoid dendritic cells (pDCs) were a unique group in terms of morphology, function, and transcription, characterized by enhanced immune stimulatory activity. Pathway analysis revealed that TNFRSF4+ pDCs primarily use OXPHOS to support their survival, proliferation, and cytotoxicity in the TME. Therefore, our results suggest that, in HNSCC, the TNFRSF4-mediated immune response plays a critical role, and OXPHOS provides essential support during this process.

We pursued the differential analysis of PS score and immune-related gene expression. The results showed a notable rise in the gene expression of indoleamine 2,3-dioxygenase 1 (IDO1) and neuropilin 1 (NRP1) within the high PS score category. IDO1, one of the three enzymes within cells (IDO1, IDO2, and TDO), has a vital function in the breakdown of tryptophan [41]. Numerous studies have emphasized its ability to suppress the immune system, which assists tumors in evading immune responses [42]. Within the TME, tumor cells and various immune cells, including stromal cells, lymphocytes, and dendritic cells, all manifest IDO1 expression. The decrease in tryptophan and the increase in its metabolites, facilitated by IDO1, lead to the dysfunction and programmed cell death of effector T cells, in addition to the stimulation of Tregs [43]. It is worth mentioning that epacadostat, a specific oral compound, hinders IDO1 and has demonstrated in preclinical studies its ability to boost the growth of effector T cells and natural killer cells, while decreasing the activation of Tregs. This effect is particularly evident when epacadostat is combined with other immunosuppressive drugs [44]. Therefore, by targeting TNFRSF4 on tumor Tregs and inhibiting IDO1, it is possible to impede tumor immune evasion and enhance the expansion of effector T cells, ultimately leading to an anti-tumor response. NRP1 has been identified as a significant promoting factor for the occurrence and development of HNSCC in our previous studies, yet its role in tumor immunotherapy, particularly its relationship with TNFRSF4, warrants further investigation and may present a potential treatment point that is often overlooked [45]. The analysis indicated a notably higher level of immune cell infiltration in the high PS expression category, specifically involving effector T cells such as CD4+ and CD8+ T cells, indicating a more robust immune response in HNSCC among individuals with high PS expression. Extensive research has been conducted on the involvement of T cell-mediated immune responses in solid tumors. Mandal *et al.* [46] used TCGA to analyze the transcriptome data of 280 tumors and comprehensively described the immune microenvironment of HNSCC. Their study highlighted that among the 10 tumors with the highest T cell infiltration, the ratio of Tregs to CD8+ T cells was highest in HNSCC (HPV+ higher than HPV–). When comparing various locations, it was observed that oropharyngeal tumors had greater infiltration of T cells compared to other tumors in the head and neck region, as well as higher infiltration of Treg cells. The lower CD8+/Treg ratio indicates that oropharyngeal tumors may be subjected to higher levels of immune regulation, suggesting that these patients may benefit from immunostimulant therapy.

We further examined the connection between the mutation spectrum of HNSCC patients in the TCGA database and their PS grouping, analyzing the available somatic mutation data. Our findings revealed that the TP53 gene had a mutation rate of over 70% in both high and low PS groups. Furthermore, the TTN, FAT1, and CDKN2A genes exhibited higher mutation rates in the high PS group when compared to the low PS group. Previous studies identified significant differences in the mutation spectrum of tumors in different subsites of the oral cavity, larynx, and other tumor subregions [47–50], with differing mutations often linked to differences in prognosis. Tumors can be vulnerable to cytotoxic therapy and may exhibit phenotypes such as an increased tumor mutation burden (TMB) due to deficiencies in DNA repair capacity and the absence of cell cycle checkpoints, which are associated with a response to immune checkpoint inhibition (ICI). Alexander *et al.* [51] discovered that mutations in tumor suppressor genes and checkpoint mediators such as TP53 and CDKN2A were prevalent in HPV-negative HNSCC. The frequency of concurrent CDKN2A mutations with TP53 mutations varied depending on the tumor subsite of HNSCC, with the highest frequency seen in laryngeal and oral cavity tumors. In early-stage tumors, the frequencies of TP53 and CDKN2A mutations, along with the likelihood of their co-occurrence, were not significantly elevated compared to advanced tumors, confirming the early onset of these mutation patterns in tumor events. Our findings suggest that these mutated genes might serve as potential research directions for ICI, especially in HNSCC.

Despite effectively employing extensive databases and artificial intelligence to examine the morphological attributes of digital pathology slides and confirm TNFRSF4 expression, our study has certain constraints. These include the limited scope of the TCGA public database and notable disparities in data and image presentation, which may impact the assessment of pathological image characteristics and their correlation with the prognosis of HNSCC patients. Furthermore, pathologists examine both the macroscopic and microscopic perspectives of every region in WSIs and choose the most illustrative perspectives to build models, thereby introducing a certain degree of selection bias. Despite these limitations, our prognostic model still demonstrates satisfactory performance, indicating that the pathological models constructed from WSIs have broad applicability.

Conclusions

The findings of our research show that histopathological image features have significant potential to predict specific gene expression and overall survival rates in HNSCC. Combining image characteristics and gene expression can effectively predict the prognosis of patients with HNSCC. The utilization of our suggested model for evaluating the prognosis of HNSCC, which relies on the expression of TNFRSF4, proves beneficial in categorizing risk levels and tailoring individualized treatment. Nevertheless, in order to corroborate the effectiveness of our model, additional pathological histology images and genetic data are imperative.

Disclosures

1. Institutional review board statement: The study was approved by the Ethics Committee of Northern Jiangsu People's Hospital Affiliated to Yangzhou University (No.: 2022ky036).
2. Assistance with the article: The authors would like to thank the TCGA working group for offering the slide images and the corresponding cancer information.
3. Financial support and sponsorship: This work was supported by the National Natural Science Foundation of China (81602188), the Science Research Foundation of Clinical Medical School, Yangzhou University (SBKY21001).
4. Conflicts of interest: None.

References

1. Johnson DE, Burtness B, Leemans CR, et al. Head and neck squamous cell carcinoma. Nat Rev Dis Primers 2020; 6: 92.
2. Bray F, Ferlay J, Soerjomataram I, et al. Global cancer statistics 2018: GLOBOCAN estimates of incidence and mortality worldwide for 36 cancers in 185 countries. CA Cancer J Clin 2018; 68: 394-424.
3. Pignon JP, le Maitre A, Maillard E, et al. Meta-analysis of chemotherapy in head and neck cancer (MACH-NC): an update on 93 randomised trials and 17,346 patients. Radiother Oncol 2009; 92: 4-14.
4. Qi Z, Liu Y, Mints M, et al. Single-cell deconvolution of head and neck squamous cell carcinoma. Cancers (Basel) 2021; 13.
5. Puntigam LK, Jeske SS, Gotz M, et al. Immune checkpoint expression on immune cells of HNSCC patients and modulation by chemo- and immunotherapy. Int J Mol Sci 2020; 21.
6. Bell RB, Leidner RS, Crittenden MR, et al. OX40 signaling in head and neck squamous cell carcinoma: Overcoming immunosuppression in the tumor microenvironment. Oral Oncol 2016; 52: 1-10.
7. Petty JK, He K, Corless CL, et al. Survival in human colorectal cancer correlates with expression of the T-cell costimulatory molecule OX-40 (CD134). Am J Surg 2002; 183: 512-518.
8. Weinberg AD, Rivera MM, Prell R, et al. Engagement of the OX-40 receptor in vivo enhances antitumor immunity. J Immunol 2000; 164: 2160-2169.
9. Li H, Chen L, Zeng H, et al. Integrative analysis of histopathological images and genomic data in colon adenocarcinoma. Front Oncol 2021; 11: 636451.
10. Zeng H, Chen L, Huang Y, et al. Integrative models of histopathological image features and omics data predict survival in head and neck squamous cell carcinoma. Front Cell Dev Biol 2020; 8: 553099.
11. Li Y, Du P, Zeng H, et al. Integrative models of histopathological images and multi-omics data predict prognosis in endometrial carcinoma. PeerJ 2023; 11: e15674.
12. Kuss I, Hathaway B, Ferris RL, et al. Decreased absolute counts of T lymphocyte subsets and their relation to disease in squamous cell carcinoma of the head and neck. Clin Cancer Res 2004; 10: 3755-3762.
13. Bauernhofer T, Kuss I, Henderson B, et al. Preferential apoptosis of CD56dim natural killer cell subset in patients with cancer. Eur J Immunol 2003; 33: 119-124.
14. Schaefer C, Kim GG, Albers A, et al. Characteristics of CD4+CD25+ regulatory T cells in the peripheral circulation of patients with head and neck cancer. Br J Cancer 2005; 92: 913-920.
15. Jie HB, Gildener-Leapman N, Li J, et al. Intratumoral regulatory T cells upregulate immunosuppressive molecules in head and neck cancer patients. Br J Cancer 2013; 109: 2629-2635.
16. Bansal-Pakala P, Halteman BS, Cheng MH, et al. Costimulation of CD8 T cell responses by OX40. J Immunol 2004; 172: 4821-4825.
17. Polesso F, Sarker M, Weinberg AD, et al. OX40 agonist tumor immunotherapy does not impact regulatory T cell suppressive function. J Immunol 2019; 203: 2011-2019.
18. Nuebling T, Schumacher CE, Hofmann M, et al. The immune checkpoint modulator OX40 and its ligand OX40L in NK-cell immunosurveillance and acute myeloid leukemia. Cancer Immunol Res 2018; 6: 209-221.
19. Aspeslagh S, Postel-Vinay S, Rusakiewicz S, et al. Rationale for anti-OX40 cancer immunotherapy. Eur J Cancer 2016; 52: 50-66.
20. Bansal-Pakala P, Jember AG, Croft M. Signaling through OX40 (CD134) breaks peripheral T-cell tolerance. Nat Med 2001; 7: 907-912.
21. Lai C, August S, Albibas A, et al. OX40+ regulatory T cells in cutaneous squamous cell carcinoma suppress effector T-cell responses and associate with metastatic potential. Clin Cancer Res 2016; 22: 4236-4248.
22. Marabelle A, Kohrt H, Sagiv-Barfi I, et al. Depleting tumor-specific Tregs at a single site eradicates disseminated tumors. J Clin Invest 2013; 123: 2447-2463.
23. Xie F, Wang Q, Chen Y, et al. Costimulatory molecule OX40/OX40L expression in ductal carcinoma in situ and invasive ductal carcinoma of breast: an immunohistochemistry-based pilot study. Pathol Res Pract 2010; 206: 735-739.
24. Bulliard Y, Jolicoeur R, Zhang J, et al. OX40 engagement depletes intratumoral Tregs via activating FcgammaRs, leading to antitumor efficacy. Immunol Cell Biol 2014; 92: 475-480.
25. Coudray N, Ocampo PS, Sakellaropoulos T, et al. Classification and mutation prediction from non-small cell lung cancer histopathology images using deep learning. Nat Med 2018; 24: 1559-1567.
26. Kim RH, Nomikou S, Coudray N, et al. Deep learning and pathomics analyses reveal cell nuclei as important features for mutation prediction of BRAF-mutated melanomas. J Invest Dermatol 2022; 142: 1650-1658.e6.
27. Schaumberg AJ, Sirintrapun SJ, Al-Ahmadie HA, et al. DeepScope: nonintrusive whole slide saliency annotation and prediction from pathologists at the microscope. Comput Intell Methods Bioinform Biostat (2016) 2017; 10477: 42-58.
28. Dolezal JM, Trzcinska A, Liao CY, et al. Deep learning prediction of BRAF-RAS gene expression signature identifies noninvasive follicular thyroid neoplasms with papillary-like nuclear features. Mod Pathol 2021; 34: 862-874.
29. Kather JN, Pearson AT, Halama N, et al. Deep learning can predict microsatellite instability directly from histology in gastrointestinal cancer. Nat Med 2019; 25: 1054-1056.
30. Cao R, Yang F, Ma SC, et al. Development and interpretation of a pathomics-based model for the prediction of microsatel-

lite instability in Colorectal Cancer. Theranostics 2020; 10: 11080-11091.
31. Inamura K, Fujiwara T, Hoshida Y, et al. Two subclasses of lung squamous cell carcinoma with different gene expression profiles and prognosis identified by hierarchical clustering and non-negative matrix factorization. Oncogene 2005; 24: 7105-7113.
32. Beer DG, Kardia SL, Huang CC, et al. Gene-expression profiles predict survival of patients with lung adenocarcinoma. Nat Med 2002; 8: 816-824.
33. Chen S, Jiang L, Zheng X, et al. Clinical use of machine learning-based pathomics signature for diagnosis and survival prediction of bladder cancer. Cancer Sci 2021; 112: 2905-2914.
34. Wu Y, Li Y, Xiong X, et al. Recent advances of pathomics in colorectal cancer diagnosis and prognosis. Front Oncol 2023; 13: 1094869.
35. Echle A, Grabsch HI, Quirke P, et al. Clinical-grade detection of microsatellite instability in colorectal tumors by deep learning. Gastroenterology 2020; 159: 1406-1416.e11.
36. Jiang W, Mei WJ, Xu SY, et al. Clinical actionability of triaging DNA mismatch repair deficient colorectal cancer from biopsy samples using deep learning. EBioMedicine 2022; 81: 104120.
37. Yamashita R, Long J, Longacre T, et al. Deep learning model for the prediction of microsatellite instability in colorectal cancer: a diagnostic study. Lancet Oncol 2021; 22: 132-141.
38. Bilal M, Raza SEA, Azam A, et al. Development and validation of a weakly supervised deep learning framework to predict the status of molecular pathways and key mutations in colorectal cancer from routine histology images: a retrospective study. Lancet Digit Health 2021; 3: e763-e772.
39. Huang X, Chen Z, Xiang X, et al. Comprehensive multi-omics analysis of the m7G in pan-cancer from the perspective of predictive, preventive, and personalized medicine. EPMA J 2022; 13: 671-697.
40. Poropatich K, Dominguez D, Chan WC, et al. OX40+ plasmacytoid dendritic cells in the tumor microenvironment promote antitumor immunity. J Clin Invest 2020; 130: 3528-3542.
41. Theate I, van Baren N, Pilotte L, et al. Extensive profiling of the expression of the indoleamine 2,3-dioxygenase 1 protein in normal and tumoral human tissues. Cancer Immunol Res 2015; 3: 161-172.
42. Prendergast GC. Immune escape as a fundamental trait of cancer: focus on IDO. Oncogene 2008; 27: 3889-3900.
43. Munn DH. Indoleamine 2,3-dioxygenase, tumor-induced tolerance and counter-regulation. Curr Opin Immunol 2006; 18: 220-225.
44. Spranger S, Koblish HK, Horton B, et al. Mechanism of tumor rejection with doublets of CTLA-4, PD-1/PD-L1, or IDO blockade involves restored IL-2 production and proliferation of CD8(+) T cells directly within the tumor microenvironment. J Immunother Cancer 2014; 2: 3.
45. Chu W, Song X, Yang X, et al. Neuropilin-1 promotes epithelial-to-mesenchymal transition by stimulating nuclear factor-kappa B and is associated with poor prognosis in human oral squamous cell carcinoma. PLoS One 2014; 9: e101931.
46. Mandal R, Senbabaoglu Y, Desrichard A, et al. The head and neck cancer immune landscape and its immunotherapeutic implications. JCI Insight 2016; 1: e89829.
47. Peri S, Izumchenko E, Schubert AD, et al. NSD1- and NSD2-damaging mutations define a subset of laryngeal tumors with favorable prognosis. Nat Commun 2017; 8: 1772.
48. Vossen DM, Verhagen CVM, Verheij M, et al. Comparative genomic analysis of oral versus laryngeal and pharyngeal cancer. Oral Oncol 2018; 81: 35-44.
49. Kim HAJ, Zeng PYF, Shaikh MH, et al. All HPV-negative head and neck cancers are not the same: analysis of the TCGA dataset reveals that anatomical sites have distinct mutation, transcriptome, hypoxia, and tumor microenvironment profiles. Oral Oncol 2021; 116: 105260.
50. Sorgini A, Kim HAJ, Zeng PYF, et al. Analysis of the TCGA dataset reveals that subsites of laryngeal squamous cell carcinoma are molecularly distinct. Cancers (Basel) 2020; 13.
51. Deneka AY, Baca Y, Serebriiskii IG, et al. Association of TP53 and CDKN2A mutation profile with tumor mutation burden in head and neck cancer. Clin Cancer Res 2022; 28: 1925-1937.

Address for correspondence:

Aijun Guo
Department of Stomatology
Northern Jiangsu People's Hospital
No. 98 Nantong West St.
Yangzhou, P.R. China
e-mail: aijunguoyzu@gmail.com